Materials Science and Engineering C 58 (2016) 420–431

Contents lists available at ScienceDirect

Materials Science and Engineering C

journal homepage: www.elsevier.com/locate/msec

Synthesis and characterization of Ti–Ta–Nb–Mn foams

C. Aguilar [a,*], C. Guerra [a], S. Lascano [b], D. Guzman [c], P.A. Rojas [d], M. Thirumurugan [a], L. Bejar [e], A. Medina [e]

[a] *Departamento de Ingeniería Metalúrgica y Materiales, Universidad Técnica Federico Santa María, Av. España 1680, Valparaíso, Chile*
[b] *Departamento de Ingeniería Mecánica, Universidad Técnica Federico Santa María, Av. España 1680, Valparaíso, Chile*
[c] *Departamento de Metalurgia, Universidad de Atacama, Av. Copayapu 485, Copiapó, Chile*
[d] *Escuela de Ingeniería Mecánica, Facultad de Ingeniería, Pontificia Universidad Católica de Valparaíso, Av. Los Carrera, 01567 Quilpué, Chile*
[e] *Universidad Michoacana de San Nicolás de Hidalgo, Ciudad Universitaria, Morelia, Michoacán, Mexico*

ARTICLE INFO

Article history:
Received 18 February 2015
Received in revised form 6 August 2015
Accepted 25 August 2015
Available online 1 September 2015

Keywords:
Ti–Nb–Ta–Mn alloys
Metallic foams
Powder metallurgy
Transmission electron microscopy

ABSTRACT

The unprecedented increase in human life expectancy have produced profound changes in the prevailing patterns of disease, like the observed increased in degenerative disc diseases, which cause degradation of the bones. Ti–Nb–Ta alloys are promising materials to replace the damaged bone due to their excellent mechanical and corrosion resistance properties. In general metallic foams are widely used for medical application due to their lower elastic moduli compare to bulk materials. In this work we studied the synthesis of 34Nb–29Ta–xMn (x: 2, 4 and 6 wt.% Mn) alloy foams (50% v/v) using ammonium hydrogen carbonate as a space holder. Alloys were produced through mechanical alloying in a planetary mill for 50 h. Green compacts were obtained by applying 430 MPa pressure. To remove the space holder from the matrix the green compacts were heated to 180 °C for 1.5 h and after sintered at 1300 °C for 3 h. Foams were characterized by x-ray diffraction, scanning, transmission electron microscopy and optical microscopy. The elastic modulus of the foam was measured as ~30 GPa, and the values are almost equal to the values predicted using various theoretical models.

1. Introduction

Biomedical and technological developments have rapidly improved life expectancy of human beings causing an increase in degenerative disc diseases by weakening the human bones. Geetha el al. [1] have reported that 90% of the population (over 40 years of age) is affected by degenerative disc diseases which will increase the total number of joint replacements by 170% in 2030. Artificial biomaterials present themselves as suitable materials to solve such problems, but their performance in time need to be proven without presenting any failure. In consequence, it is very important to develop materials with high longevity, adequate mechanical properties and excellent bio-compatibility. Metallic materials are widely used as implants under load-bearing conditions [2,3]. The first metallic materials used as surgical implants were 316L stainless steels (316LSS), Co–Cr alloys, Co–Cr–Mo alloys. Such alloys have few disadvantages like high elastic modulus (E) around 200 GPa, which is very high compared with the E values of cortical bones, with around 2 to 30 GPa [1,4]. Nowadays, pure Ti and Ti alloys are widely used as bio-implant materials because of their excellent properties even though their E values are higher (around 110 GPa) than the human bones [1,4]. The first generation of Ti alloys had several disadvantages such as relatively poor wear resistance, lower hardness and higher stiffness than human bones [5,6]. The stiffness mismatch between the implant materials and human bones causes bone resorption and eventual loosening of the implants [2,3]. Also, few alloying elements such as Al, V, Ni and Co present in the Ti alloys produce toxic effects when they are placed into the human body. Some diseases produced by these elements are dermatitis, Alzheimer, neuropathy and osteomalacia [7–9]. A second generation of Ti alloys was produced with non-toxic elements such as Nb, Mo, Zr or Ta [10]. However these alloys present problems associated with their mechanical and corrosion performances. Efforts need to be directed towards finding new alloying elements with improved properties. It has been reported that alloying element Mn has a special role as a co-factor in the bone mineralization and bone cartilage and collagen formation [11]. Ti–Mn alloys are commonly used as aerospace materials but not as bio-materials. Nicula et al. [12] have reported that the Mn in Ti–Al–V alloys could enhance cell adhesion to such materials. Only few reports have studied the effect of Mn on Ti alloys, especially in their second generation. β-phase Ti alloys are preferred as bio-implant materials, because their elastic modulus are smaller than the α or (α + β) phases [13]. β-phase Ti alloys are formed by incorporating β-stabilizing elements such as Pd, Ni, Mo, Ta, V, Mn, and Nb [14].

The elastic modulus (E) of materials may vary depending on the nature of atomic bonding. Typical approaches to decrease the E values are: i) formation of solid solutions, ii) synthesis of composite materials and

---

[*] Corresponding author at: Departamento de Ingeniería Metalúrgica y Materiales, Universidad Técnica Federico Santa María, Av. España 1680 , Valparaíso, Chile.
E-mail address: claudio.aguilar@usm.cl (C. Aguilar).

http://dx.doi.org/10.1016/j.msec.2015.08.053
0928-4931/

Table 1
Methods of synthesis of metallic foams [21].

Closed pores		Open pores		
Random pore distribution	Graded pore distribution	Non-homogeneous	Homogeneous	Functionally graded
Gas injection into the metal met	Plasma spraying	Sintered metal powders	Orderly oriented wire mesh	Rapid prototyping
Decomposition of foaming agents		Sintered metal fibers	Vapor deposition	Electro discharge compaction
		Space holder method	Ferromagnetic fiber array	
		Replication	Rapid prototyping	
		Combustion synthesis		
		Plasma spraying		

iii) synthesis of foams (which have two types of pores; closed and open pores). For biomedical application, foams with open pores are preferred for the increased growth of tissue and cells on the surface of the material. In general, metallic foams with open pores can be produced by three routes; solid state in powder or fiber form, liquid metal and metal vapor or gaseous metallic compound. Based on the pores and porosity levels, E values of metallic foams can be customized to match the elastic modulus of the bone to reduce problems associated with the stress shielding. Table 1 summarizes the methods to produce foams with different type and distribution of porosity. Method's choice will depend on the type, distribution and sizes of pores required for the needed bio-material. Foams can be designed using theoretical models such as Gibson and Ashby [15], Nielsen [16], Knudsen [17], Spriggs [18], Phani and Niyogi [19] and Pabst and Gregorova [20] that predict E values based in porosity and other physical parameters.

When processing Ti foams, powder metallurgy (PM) method is highly preferred over than casting, forging and other mechanical techniques [14]. For instance, during casting process, Ti alloys become highly reactive at temperatures higher than 600 °C and also it is prone to rapid oxidation [14]. Therefore, high vacuum furnaces are required to synthesize Ti alloys which involves more difficulty and high cost. PM method, in contrast, can be performed even at low temperatures, making it ideal for processing Ti foams. By PM the following methods are used to synthesize the foams; sintered metal powders [22] and space holder [23–25]. In this work, synthesis of Ti–34Nb–29Ta–xMn (x: 2, 4 and 6 wt.%) foams by powder metallurgy space holder technique is investigated (NH_5CO_3 was used as space holder). The effect of the amount of Mn on the porosity, pore size, phase constitution and elastic modulus in compression of the foams was investigated. Also elastic modulus values were calculated using different theoretical models.

2. Materials and methods

Ti powders of grade IV (−100 mesh, Goodfellow, UK), Ta powders (99.9% purity, −325 mesh, Noah USA), Nb powders (99.9% purity, −325 mesh, Noah USA) and Mn powders (99.7% purity, −100 to +200 mesh, Noah USA) were chosen to produce the powder blends of Ti–34Nb–29Ta–xMn (x: 2, 4 and 6 wt.% Mn). The mixture was placed in 250 ml hardened steel vial and milled in an argon atmosphere (ultra-pure with 99.999% with <2 ppm O_2) using a planetary mill. 2 wt.% of stearic acid was added as lubricant to the milling process. The powders were milled for 50 h using different diameters of hardened steel balls (15, 12.5, 11, 8.0 and 6.5 mm of diameters) with a constant ball/powder ratio of 10/1. Fig. 1 shows the schematic steps of space holder method.

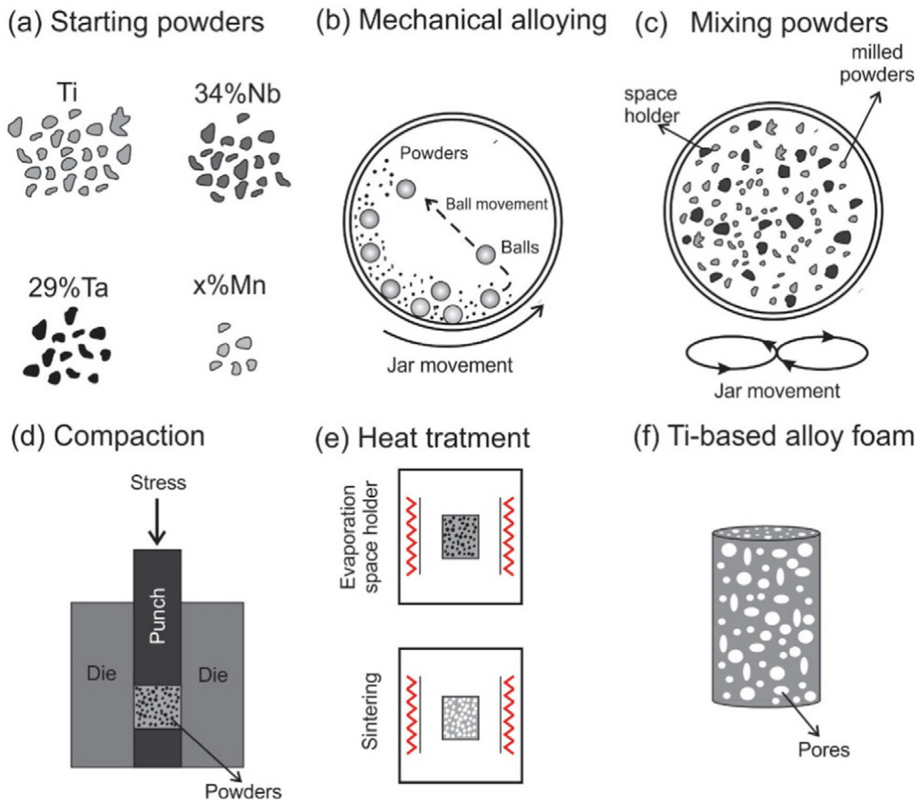

Fig. 1. Scheme of synthesis of metallic foams by means of space holder method.

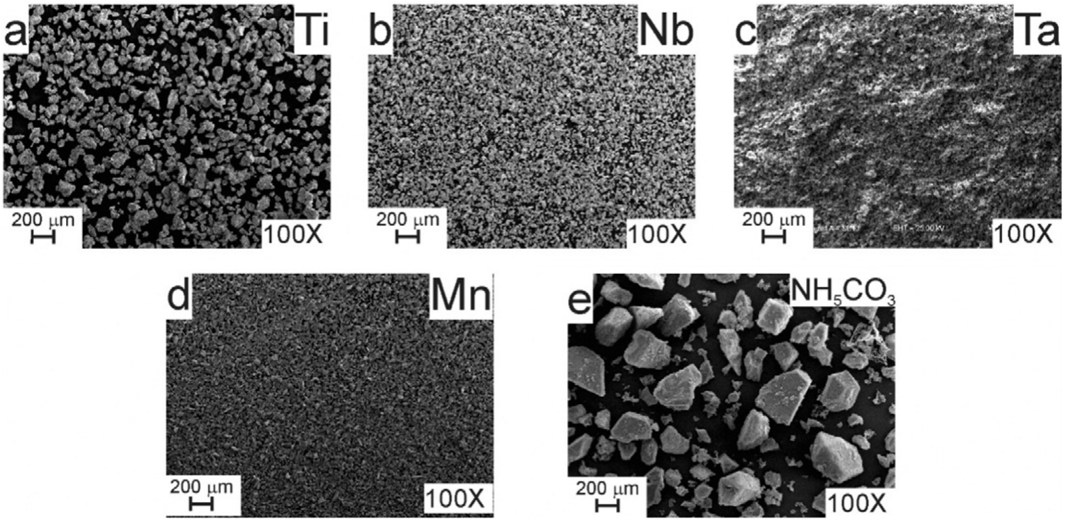

Fig. 2. Morphology and size of as-received powders, (a) titanium, (b) niobium, (c) tantalum, (d) manganese and (e) ammonium hydrogen carbonate.

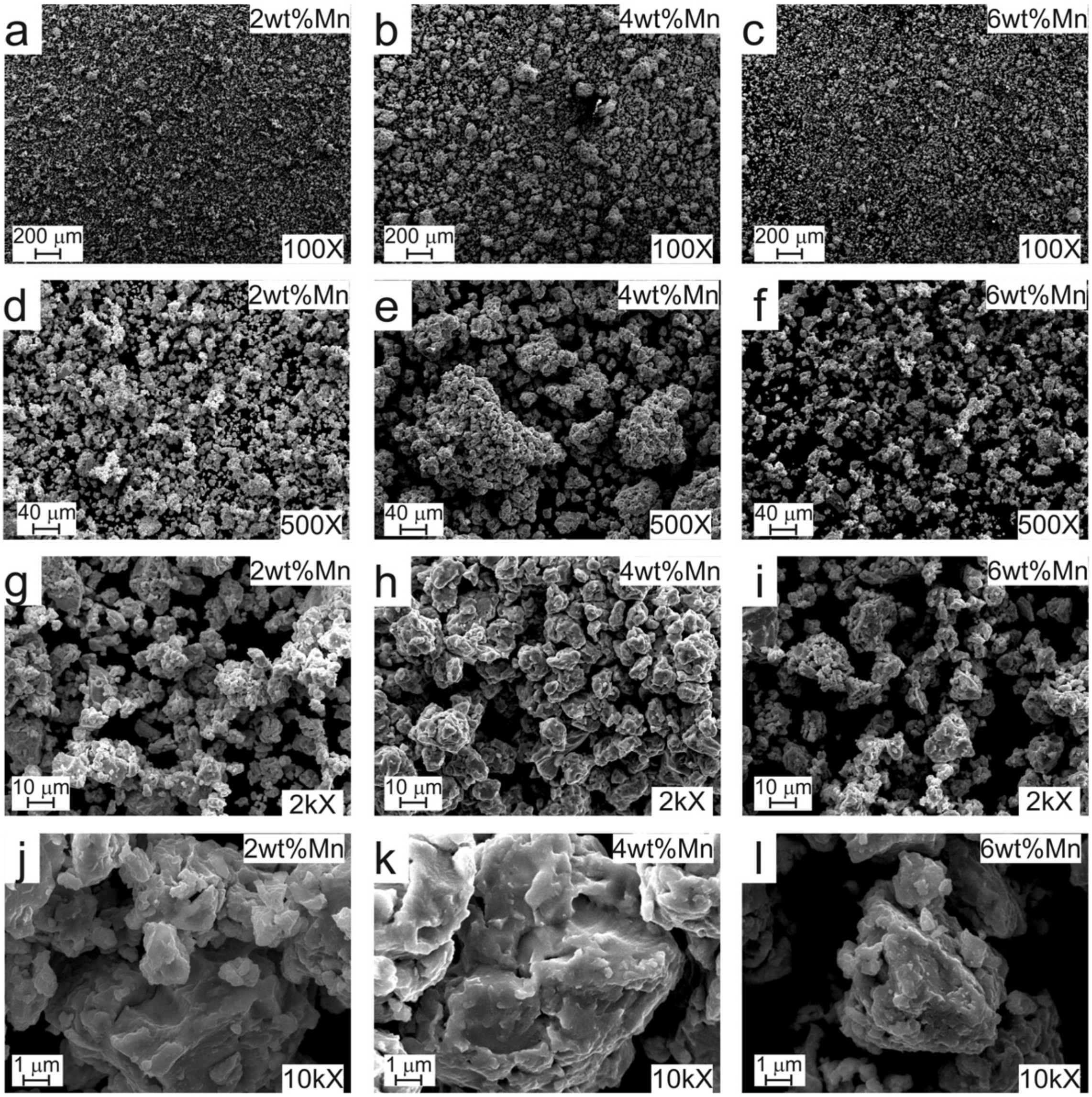

Fig. 3. SEM images of milled powder at 50 h for Ti–34Nb–29Ta–xMn (x: 2, 4, 6 wt.%) alloys.

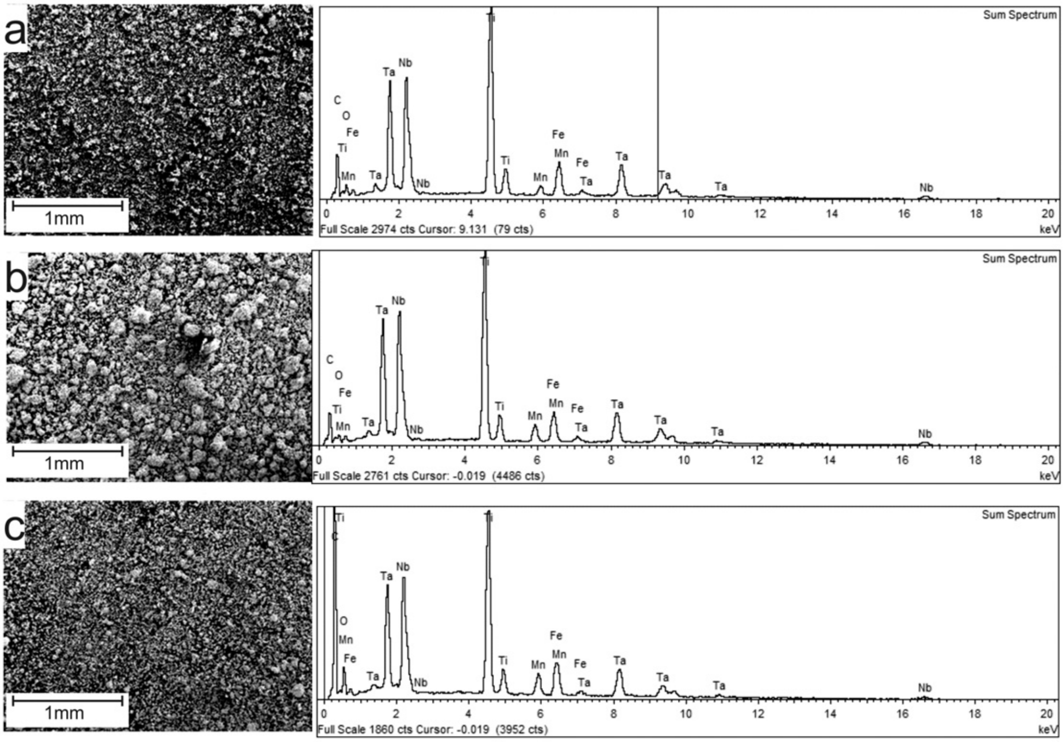

Fig. 4. EDS analysis of Ti–34Nb–29Ta–xMn (x: 2, 4, 6 wt.%) powders milled during 50 h.

The milled powders were mixed with ammonium hydrogen carbonate (NH_5CO_3) at 50% v/v to produce samples of 50% porosity level. From such mixture, cylindrical samples of 13 mm of diameter and 25 mm of height were compacted in an universal testing machine zwick roel Z030 using uniaxial compaction (430 MPa). The green compacts were initially heated at 180 °C for 1.5 h to eliminate NH_5CO_3, then heated at 1300 °C for 3 h, followed by natural furnace cooling down. The milled powders and foams were characterized by using different techniques.

2.1. Characterization of powders

The x-ray diffraction (XRD) analysis of milled powders was performed using a Shimatzu diffractometer with copper target. All patterns were measured in an angular range between 30 and 120° (2θ). As-received milled powders and foams were observed by a scanning electron microscopy (SEM) Zeiss EVO MA 10. Composition was characterized by energy dispersive x-ray spectroscopy (EDS). In addition, transmission electron microscopy measurements were performed through a FEI Tecnai of 200 kV microscope. TEM samples were prepared by suspending the powders in isopropyl alcohol and placing a drop on a Cu grid.

2.2. Characterization of sintered foams

The porosity of sintered foams was measured by the standard ASTM C373 method and through the image analysis software supplied by Leica microscope. For optical analysis, foam specimens were ground by increasing grades silicon carbide paper (320, 400, 600 and 1000-grit). Cloth polishing consisted of two stages, at a first stage 9 μm diamond particles + water was used for 20 min followed by a second stage where magnesium oxide + hydrogen peroxide (30%) was used for 20 to 60 min. Additionally, compression testing to evaluate samples elastic modulus were performed in an universal testing machine Zwick Roell Z030 at a strain rate of 0.125 mm/min. These results were compared with theoretical models.

3. Results and discussion

3.1. Characterization of powders

Fig. 2 shows size and morphologies of starting materials used in synthesizing the metallic foam. Ti, Nb and Mn powders showed irregular shapes with grain size smaller than 150 μm, 45 μm and 45 μm, respectively. Ta powder showed a rounded, irregular morphology with grain size smaller than 45 μm. Observed particle size of NH_5CO_3 was smaller

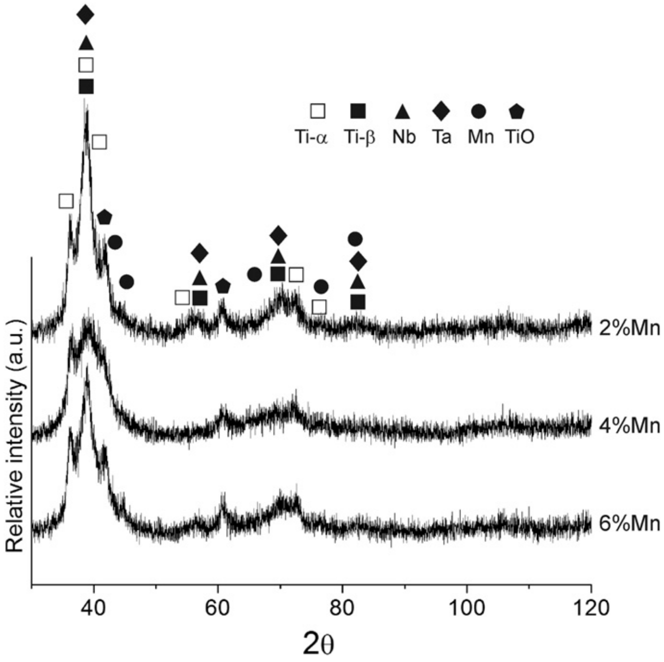

Fig. 5. Whole XRD pattern of Ti–30Nb–13Ta–xMn (x: 2, 4, 6 wt.%) powder.

than 600 μm which was notoriously larger than metallic milled particles.

Fig. 3 shows morphologies and grain size of Ti–34Nb–29Ta–xMn alloy (x: 2, 4, 6 wt.%) powders after 50 h of milling. Observed agglomerated particle sizes was 60 μm, 200 μm and 40 μm for 2, 4 and 6% Mn, respectively. Agglomerated particle size is larger for alloys containing 4% Mn because agglomeration effect was higher for this concentration (Fig. 3e). The alloys containing 2 and 6% Mn showed agglomerated particles with irregular shapes whereas 4% Mn showed more equiaxed particles. In MA, energy transferred from balls to powder generates a smaller grain size, increased grain boundary surface area and increased crystalline defects density. Milling created new surfaces, enabling particles to weld together leading to an increased agglomerated particle size [26]. The surface tension of powders was modified by the different amount of Mn added in milling process. Powders containing 4% Mn reached a high surface tension value which leads to larger agglomerated particles. Powder particle edges were smooth in the alloy containing 4% Mn because cold welding dominated over fracture (Fig. 3k). Powders containing 2% and 6% Mn exhibit less surface tension and the powder particle edges were rough as evidence that fracture predominates over cold welding (Fig. 3j and l). As milling time increases, powder particle brittleness increases as a result of work-hardening and the particle size decreases until the fracture strength of particles are equal or greater to the stress caused by the collision [27]. In consequence, if the milling time increases the level of contamination increases as well. Fig. 4 shows the EDS analysis of three alloys, which revealed iron and oxygen contamination due to the impact of balls and vial.

Fig. 5 shows the XRD patterns of powders milled for 50 h. No intermetallic compounds of Ti, Nb, Ta or Mn were observed although TiO peaks detected. The strongest peaks corresponding to Nb (110), Ta (110) and Mn (221) disappeared after 50 h milling time. The disappeared peaks of solute Nb, Ta and Mn is assumed to be the formation of a solid solution [26]. In addition, obtained XRD patterns exhibited an amorphous phase, which will be interesting for the further studies. Observed Ti and Mn peaks in the amorphous hump are in agreement to a mixed crystalline and an amorphous phases. The peak broadening, peak shift and disappearance of solute peaks are commonly observed as a result of MA. XRD peaks increase their broadening when materials are under severe strain and nano-sized crystals are formed. If milling time increases, the crystallite size decreases steadily and shear band coalesces. When strain increases grain boundaries angle become larger, a clear sign of grain rotation which produces disclinations [28]. This is reflected in an absence of texture in the electron diffraction pattern and an observed random orientation of the grains (contributing to x-

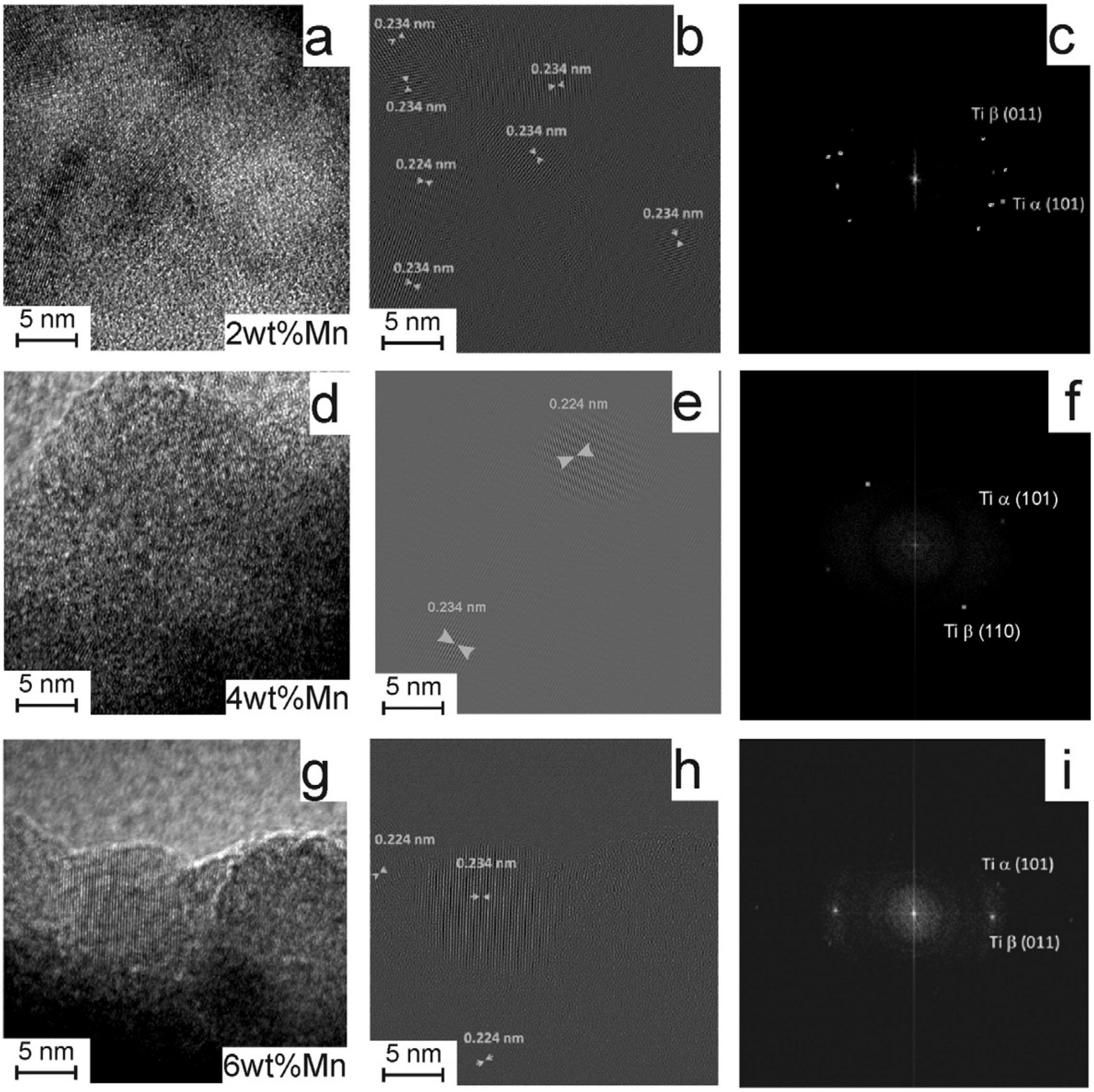

Fig. 6. (a), (d), (g) TEM images of Ti-based alloys, (b), (e), (h) FFT and (c), (f), (i) diffraction patterns.

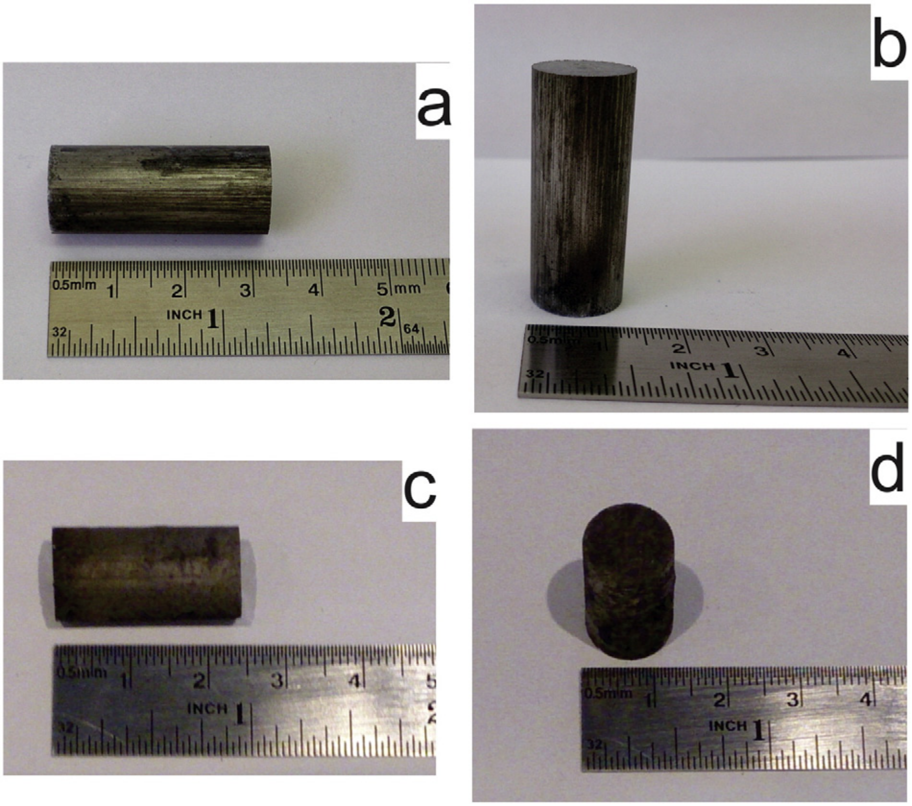

Fig. 7. Photographs of (a), (b) green and (c), (d) sintered samples for Ti–30Nb–13Ta–4Mn alloys.

ray peak diffraction broadening). As the milling process progresses, the nanocrystalline grains reach the saturation value due to the increasing difficulty in dislocation generation as nanocrystalline scale is reached. At such scale existing dislocations rearrange themselves and few of them become eliminated [26], decreasing strain and dislocation density. In nanocrystalline materials, the grain size can coincide with crystallite size, so the crystallite size is the smallest measurable scale in microstructure.

Fig. 6 shows HRTEM images of milled powders of the three alloys. Mixed zones of nanocrystalline and amorphous phases are shown in Fig. 6a,d and g. Figures b, e and h shows corresponding Inverse Fast Fourier Transform (IFFT) and Fig. 6c,f and i shows the Fast Fourier Transform (FFT). TEM images showed crystallite size smaller than 5 nm surrounded by an amorphous phases. From rings and spot inTEM images Ti-α and Ti-β phases, with hcp and bcc structures, where found. Through MA, it is possible to produce amorphous phases with different compositions [29] and make composition ranges for the amorphous phase formation wider than using any other processes [30]. The solid solution and the strain energy increases linearly with the solute content. If lattice strain reaches a critical value, amorphous phase formation becomes more favorable than a crystalline phase. During MA, powder undergoes severe plastic deformation and produce a high crystalline defect density and an increased grain boundary area. The decrease in crystallite size enhance speed of diffusion process [29] and smaller atomic volume ratio leads to the amorphous phase formation [31]. The criteria for the amorphous phase formation are different for liquid-quenching techniques such as rapid solidification processing [32] and solid-state processing techniques such as MA [33]. A common criterion observed for the formation of amorphous phase formation by all techniques is that a significant difference in atomic sizes between the constituent elements introduces strain into the alloy generating an amorphous phase [30].

3.2. Characterization of foams

Fig. 7 shows pictures of green and sintered foams. Green samples showed a smooth outer surface (Fig. 7a and b). Small oxidation was observed at the edges of sintered samples. Sintered samples undergo shrinkage effects through the sintering process (Fig. 7c and d). During sintering, diffusion occurs and a change in sample volume is observed because of the atomic rearrangement. Shrinkage effect was calculated

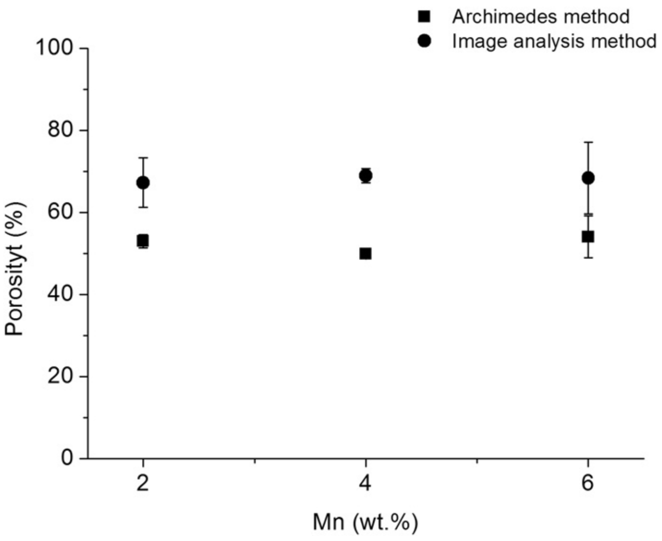

Fig. 8. Total porosity as a function of Mn content obtained by Archimedes method and image analysis.

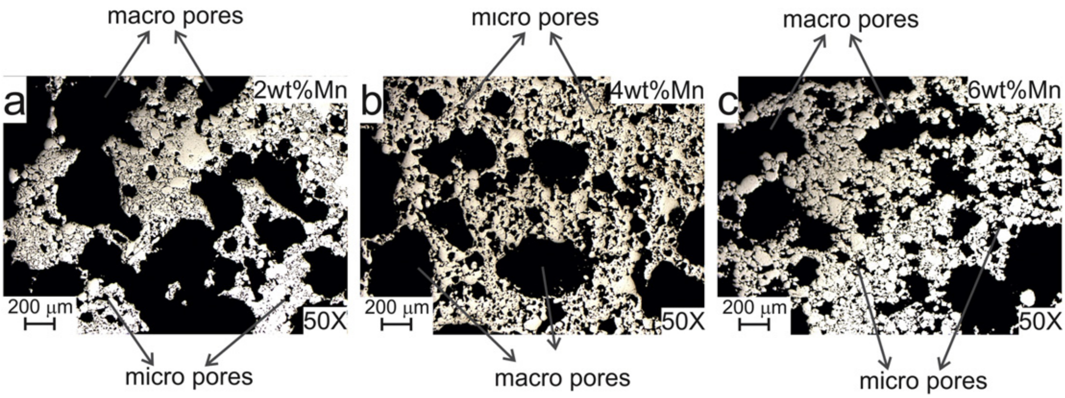

Fig. 9. Optical images of foams where big and small pores are observed.

using Eq. (1) [34] considering the external volume change of cylindrical sample, where V is original sample volume, h and r correspond to the height and radius of cylindrical sample, ΔV, Δh and Δr are the change of volume, height and radius. Calculated average exterior volume change (ΔV/V) values for 2, 4 and 6% Mn samples were −14, −25 and −17%, respectively.

$$\frac{\Delta V}{V} \approx \frac{\Delta h}{h} + \frac{2\Delta r}{r}. \tag{1}$$

The intrinsic shrinkage $(-\Delta V/V_0)_{\text{intrinsic}}$ was determined by using Eq. (2) [34], where p and p_0 are the final and initial porosity of green samples, respectively. The measured average intrinsic shrinkage values for 2, 4 and 6% Mn foams were −43, −54 and −45%, respectively. Although foams were initially designed to exhibit 50% porosity level it was necessary to measure the real porosity after sintering process. Porosity values were measured by both Archimedes's method (as per ASTM C373 standard) and through image analysis. Fig. 8 shows the porosity values measured by Archimedes method. For all % Mn content, Archimedes method showed around 50% porosity values. However, porosity values obtained by image analysis showed porosity larger than 50%, Fig. 8. These results prove that the % Mn content do not influence porosity levels of resulting the foams. Because the porosity influenced by sintering temperature and time, compaction pressure, amount and type of space holder, process control agent (PCA). Nouri et al. [35] studied porosity changes with the amount and type of PCA

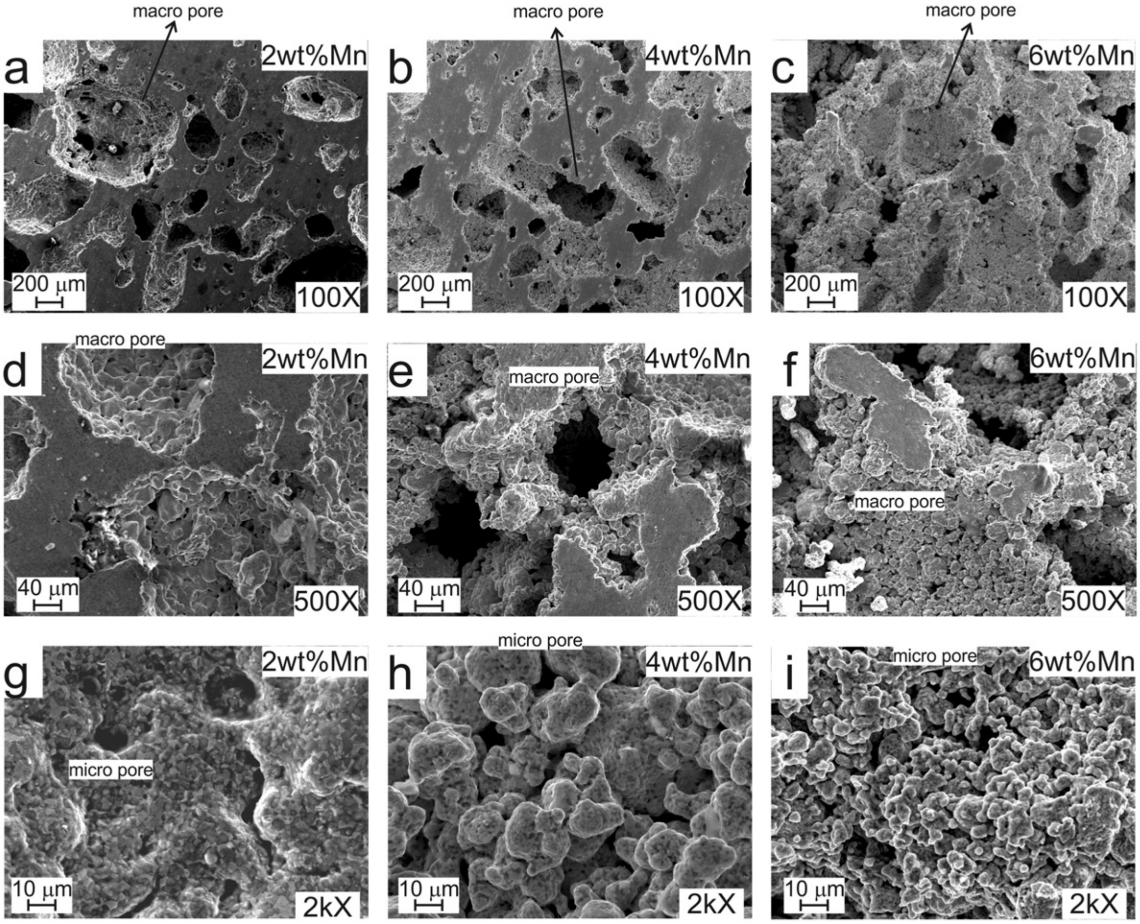

Fig. 10. SEM images of foams for different amount of Mn and magnifications.

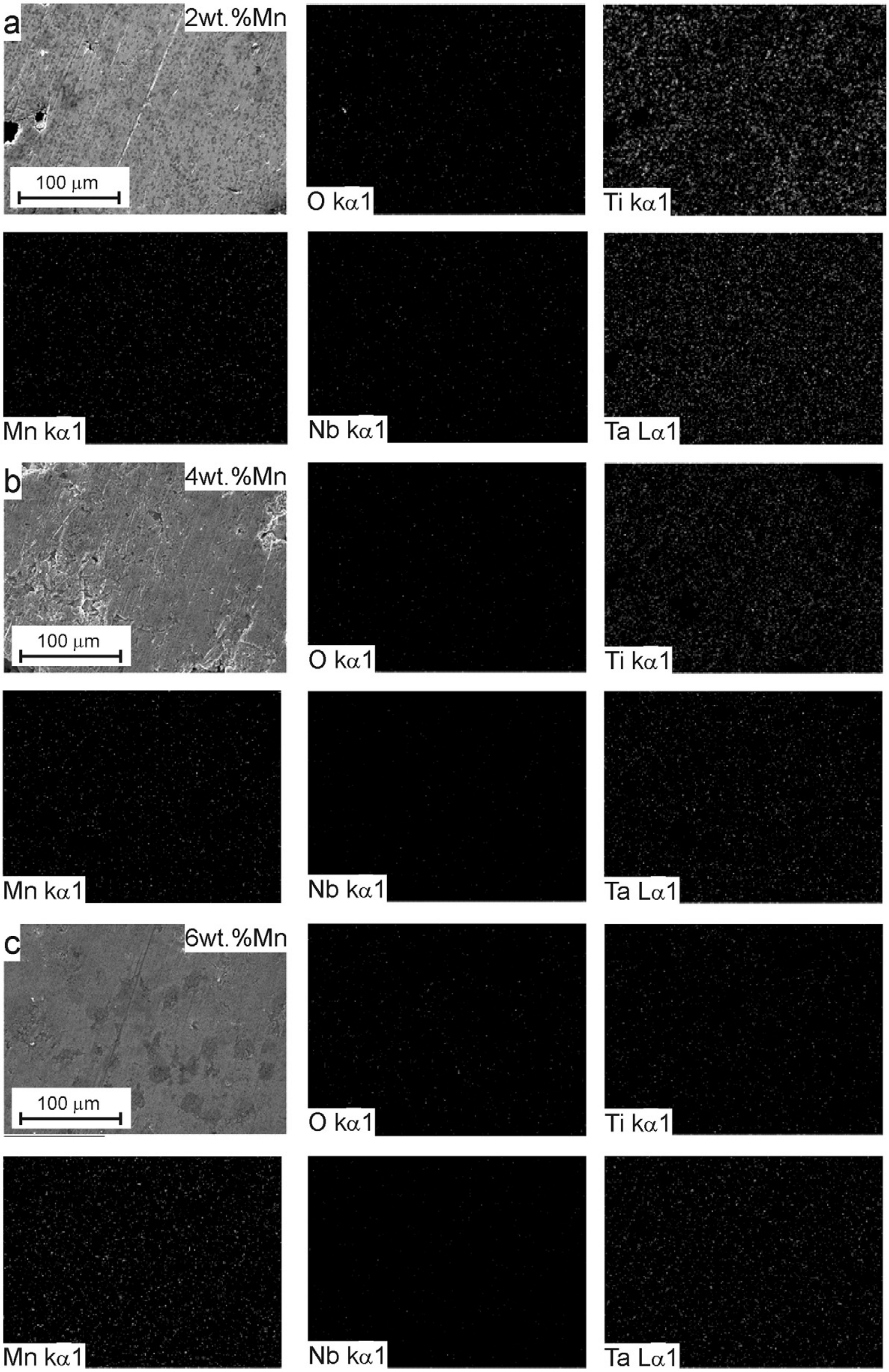

Fig. 11. Elemental distribution in metallic foams determined by EDS, (a) 2 wt.% Mn, (b) 4 wt.% Mn and (c) 6 wt.% Mn.

(stearic acid and ethylene bis stearemida), for Ti–16Sn–4Nb foams. They showed that high PCA content promoted sintering and increased interparticle bonding of porous, while absence or only 1%PCA content promoted the corrugated pore walls and large number of micropores. Also, porosity values decreased from 77 to 68% for samples containing from 0 to 3% of PCA. Ibrahim et al. [36] have reported that porosity values decreased with increasing sintering temperature and compaction pressure for c.p. Ti and Ti–5 wt.% Mn foams. Zhang et al. [37] have shown the effect of the weight ratio and particle size of NaCl on the porosity and pore size of Ti foams.

$$\left(-\frac{\Delta V}{V_0}\right)_{\text{intrinsic}} \approx p - p_0 - \frac{\Delta V}{V_0}. \tag{2}$$

Fig. 9 shows the optical images of foams with different amount of Mn. Foams exhibited a bimodal microstructure composed of macro pores and micro pores. The macro pores were produced by the space holder and micro pores were formed during the sintering process. The sizes of macro pores decreased with the increase of Mn content.

The macro and micro pores were heterogeneously distributed exhibiting irregular shape, which revealed the typical morphology of the foams produced by the space holder method [21,38]. Cell edges of macro pores were irregular in thickness and inhomogeneous in distribution. Measured average size of macro pores was smaller than 600 μm for different amount of Mn, Corresponding value for micro pores size was smaller than 20 μm (Fig. 9). The macro pores in the samples are connected by micro pores which are distributed along the cell edges of macro pores. Such bimodal porous microstructure is suitable for growth of new bone tissue and vascularization [39] whereas the rough border of pores promotes osteointegration. Analyzed results were in good agreement with previous works. Wen et al. [39] have synthesized TiZr foams by space holder method with macro pore size of 200–500 μm. Nouri et al. [35] have reported macro pores size of 350 μm for metallic foams of Ti–16Sn–4Nb alloys. Pore wall edges were rough and corrugated for samples with no process control agent and samples containing 1% of same agent. Samples containing 2 and 3% of process control agent showed rounded pores with well-defined necks. This indicates that the amount of process control agent influences morphology and configuration of the pores. Wang et al. [40] have studied the effect of NH_5CO_3 addition over Ti–10 wt.% Mg alloy foams, showing that porosities and open porosities were increased depending the concentration and particle size of NH_5CO_3.

Fig. 10 shows SEM images of foams with different magnifications. Obtained macro pore size was in the range of 100–600 μm (Fig. 7a,b and c), while micro pore sizes were smaller than 20 μm (Fig. 9g,h and i). Similar results have been reported by other authors. Xiang et al. [41] prepared titanium foams using NH_5CO_3 as space holder and produced samples with a bimodal distribution of pores (200–500 μm) which leads to micro pores with irregular in size and shape. For samples in the present study micropore size decreased with the amount of Mn, which is clearly seen in Fig. 10g,h and i. Microstructure of foams exhibits three important characteristics: i) rounded corners of macro and micro pores contributed to decrease the stress concentration, ii) macro and micro pores were interconnected (micro pores in the cell walls and edges connected to the macro pores) and, iii) the macro and micro pores showed an evident rough inner surface which could be relevant for application in bone growth. Interconnectivity, in particular, is an important criterion used to evaluate porous implants for its role in

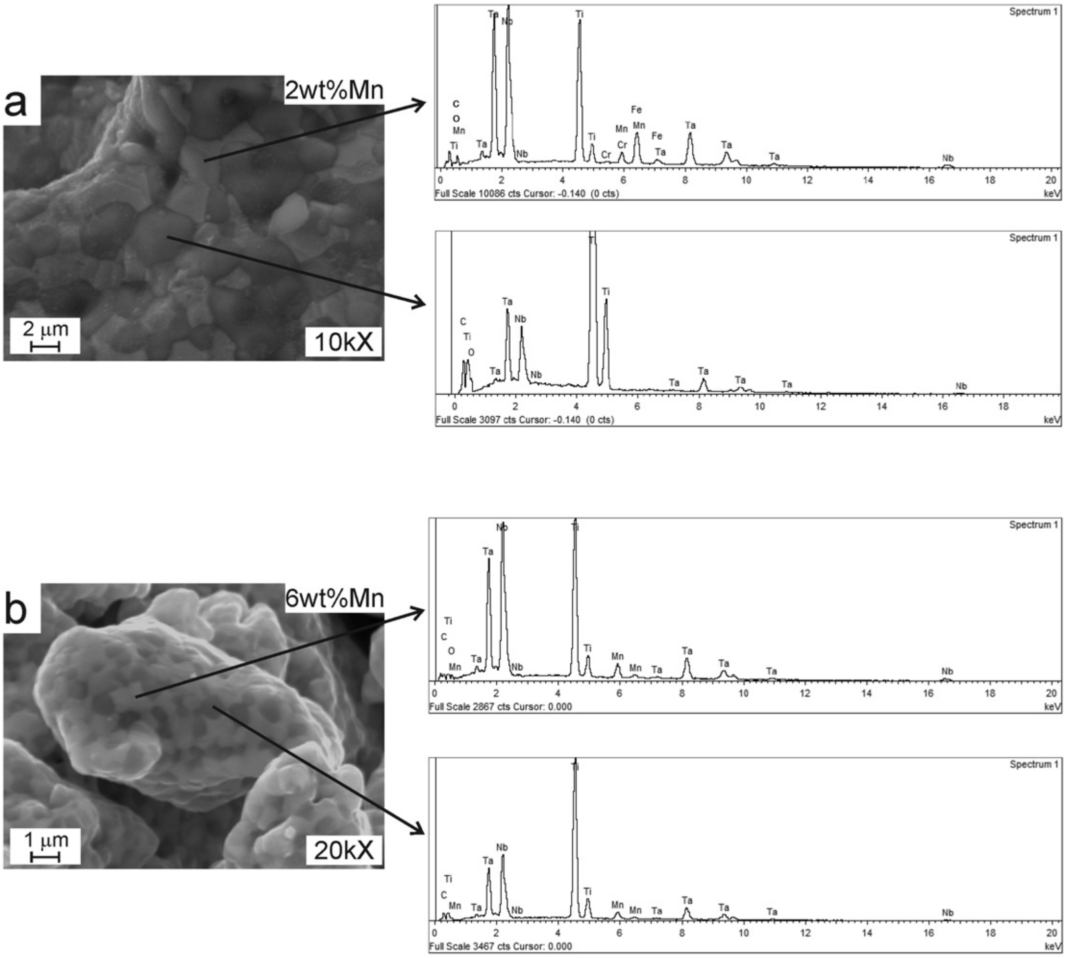

Fig. 12. EDS analysis of two phases produced in metallic foams, (a) 2 wt.% Mn and (b) 6 wt.% Mn.

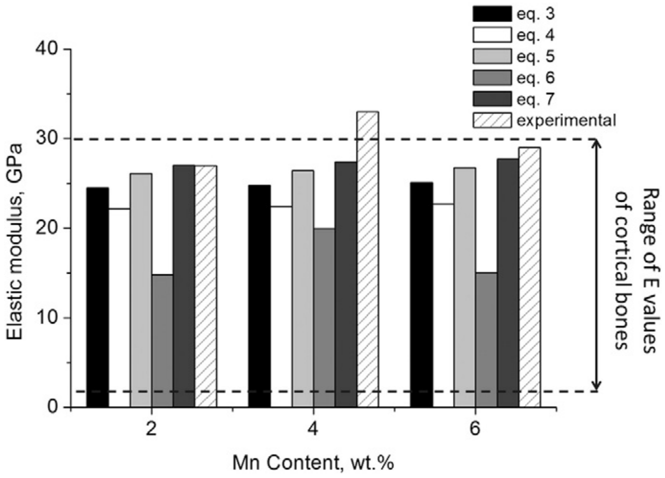

Fig. 13. Estimations of E values using different models described in text together with E value experimentally measured.

Table 2
Constant values used in different models to estimate E value.

Eq. (3)	Eq. (4)	Eq. (5)	Eq. (6)	Eq. (7)
$b = 3.36$	$m = 1.93$ $pc = 83\%$	$a = 1$ $pc = 83\%$	$\alpha = 1$ $n = 2$	$Ff = 0.7$
	2 wt.% Mn	2 wt.% Mn		2 wt.% Mn
Density, g/cc	9.53	9.55		9.57
E, GPa	131	133		134
p, %	50			

nutrition delivery and body fluid transport. Similar results were reported by Rao et al. [42] for Ti–Nb–Zr foams and Wang et al. [40] for Ti–Mg foams. Pore interconnectivity can be controlled by the space-holder shape, size and packing, sintering temperature and time and temperature of dissolution (if the space holder is salt). The pore roughness of inner surface can be controlled by the shape and size of the space holder, amount of Ti, Nb, Ta and Mn powders, temperature and sintering time. Macro pores showed a small pore aspect ratio (close to the equiaxial shape), which differs from the aspect ratio of human bones (elongated pores) [43].

Fig. 11 shows the element distribution obtained from EDS/SEM mapping method. Ti, Nb, Ta and Mn were present and spread homogeneously (at macroscopic level) for the different amount Mn foams used in this study. In addition, homogeneously distributed oxygen was detected in all foams. These results are in agreement with XRD results showed in Fig. 5.

At microscopic level two phases were found in all foams, one Ti rich and another Nb–Ta rich. From EDS analysis Ti rich phase was localized at darker areas while Nb–Ta rich phase was found at gray areas, as is highlighted in Fig. 12. When Mn content is increased in foams two effects were observed; i) size of both phases decreased; Ti rich phase size was around 4 μm for 2% Mn and 1 μm for 6% Mn (Fig. 11), and ii) amount of Mn in Nb–Ta rich phase increased. Nb, Ta and Mn elements formed the solid solution because these elements exhibit bcc-crystalline structure and are β-stabilizer. To understand phase formation in ternary Ti–Nb–Ta systems, earlier reports of their thermodynamic properties were considered. For example, Gavzeo et al. [44] studied the ternary phase of Ti–Nb–Ta system at 0 °C and Cocks et al. [45] studied the ternary phase of Ti–Nb–Ta system at 2400 °C. At 0 °C the phase diagram showed only one solid phase and at 2400 °C showed two phases; rich in solid Ta and rich in liquid Ti. Li and Warnes [46] experimentally studied the Ti–Nb–Ta ternary system at 400 and 550 °C and reported three zones: the first zone was rich in Ti (α phase), the second zone was a mix of α and β phases, and the third zone was rich in β phase Nb and Ta. Tang et al. [47] studied the phase transformations in solid solutions for treated and quenched Ti–(13–26)Nb–(22–38)Ta (wt.%) alloys. Phase transformations in such alloys were sensitive to both composition and cooling rate. The slow cooling technique showed the fine α and $\omega_{\text{isothermal}}$ formation within the β matrix and the water and oil quenching techniques resulted in the formation of orthorhombic martensite (α″) in a retained $\beta + \omega_{\text{athermal}}$ matrix. Under conditions of equilibrium, α phase microstructure volume fraction decreases while β phase increases. Cooling rate controls the microstructure when the sample is under non-equilibrium cooling condition. The α phase precipitation is formed at low cooling rates. Two martensite phases are formed through high cooling rates; (i) hexagonal (α″) structure and (ii) orthorhombic (α′) structure. When β-stabilizer content increased, the martensite transformation onset temperature (M_S) is reduced [48]. Moffat and Larbalestier [49] have studied the competition between the stable α phase and a metastable phase that precipitates in a metastable β phase matrix in aged Ti–Nb alloys. Generally above 425 °C microstructure was β + α, between 375 and 425 °C aged microstructure was β + ω (which turns β + α with prolonged aging) and below 375 °C only ω precipitates were present. Since, our heating cycle also involved natural cooling down of furnace, an equivalent effect of Ti–Nb–Ta–Mn alloys aging could be expected. The precipitation of ω phase in titanium alloys was not desirable, since it could lead to excessive embrittlement, loss of ductility and fatigue resistance [50].

To predict the elastic modulus of foams some models were proposed in earlier reports. Zhu et al. [51] proposed one general expression of the elastic modulus as a function of porosity which was expressed as $E = E_0 f(p)$, where E is the elastic modulus of the foam, E_0 is the elastic modulus of bulk material, p is the porosity and f(p) is a function that correlates the elastic modulus to the porosity that is usually obtained by fitting the experimental data. Knudsen [17] and Spriggs [18] proposed Eq. (3) to obtain E where b is a material constant that is related to particles stacking. This expression is widely used to predict the elastic

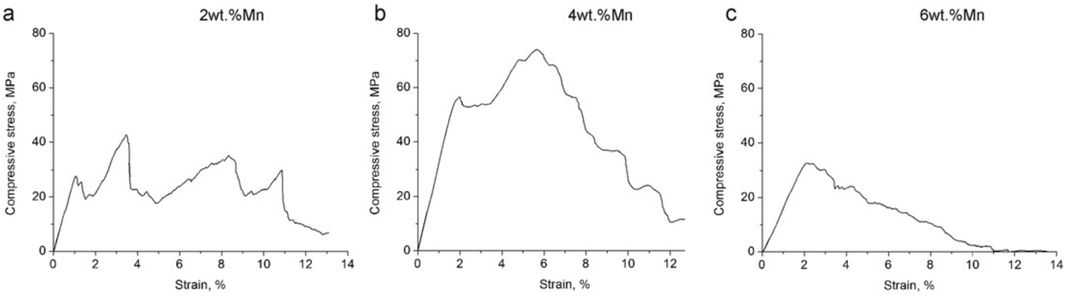

Fig. 14. Compressive stress–strain curves of metallic foams, (a) 2 wt.% Mn, (b) 4 wt.% Mn and (c) 6 wt.% Mn.

modulus of foams with low p, but does not satisfy the boundary condition that E is equal to zero for p = 1.

$$E = E_0 e^{-bp}. \tag{3}$$

Phani and Niyogi [19] proposed Eq. (4) to determine E, where p_c is the critical porosity at which E = 0, i.e. the material loose integrity. The critical porosity depend on the stacking geometry of particles, and the material constant *m* also depend on pore distribution geometry, such as shape and connectivity.

$$E = E_0 \left(1 - \frac{p}{p_c}\right)^m. \tag{4}$$

Pabst and Gregorová [20] proposed Eq. (5) which expressed E as a function of packing geometry factor (a), when pores show spherical shapes the value of *a* is 1.

$$E = E_0 (1 - a\ p) \left(1 - \frac{p}{p_c}\right). \tag{5}$$

Gibson and Ashby [15] proposed a model where E values are affected by relative density (Eq. (6)), where ρ and ρ_0 are the density of the foam and dense matrix material, respectively and C and n are constants depending on the porous structure. *n* value varies between 1.8 and 2.2 and α between 0.1 and 4, depending on the structure of metallic foam. We consider $n \approx 2$ as approximation. Xiong et al. [3] measured the mechanical properties of Ti foams and determined that C = 1 in Eq. (6).

$$E = \alpha E_0 \left(\frac{\rho}{\rho_0}\right)^n. \tag{6}$$

Nielsen [16] proposed a model to determine E values by considering the porosity and the pore shape factor (F_f), Eq. (7), where $F_f = 4pA/PE^2$, A is the pore area and PE is the experimental perimeter of the pore. In our work the F_f were measured by Pro image analysis software.

$$E = E_0 \left[\frac{(1 - p/100)^2}{1 + (1/F_f - 1)p/100}\right]. \tag{7}$$

Fig. 13 shows calculated E values using Eqs. (3)–(7). The experimental elastic moduli were estimated from stress–strain curves shown in Fig. 14. Constant values were taken from Zhu et al. report [51]. They measured E values for foams of Ti alloys with various porosities using an electromagnetic acoustic resonance experiment. Constant values used in this work are listed in Table 2. Obtained E values ranging between 15 and 28 GPa. These E values are in the upper range of the elastic modulus values of cortical bones [52].

Considering that elastic modulus of the cortical bones are different in longitudinal and transverse directions because of anisotropy, typical elastic modulus were reported as their average values.

Fig. 14 shows the compressive stress–strain curves versus Mn content. The curves did not show any typical feature of foams during compressing, i.e., elastic deformation stage, plateau stage and densification stage. In the elastic deformation stage, all pore walls were deformed elastically. Also, during elastic behavior foams exhibited two phenomena, i) high elastic deformation observed when increasing Mn content and ii) elastic modulus values do not change with Mn content. Measured elastic deformations were 1, 1,7 and 2% with 2, 4 and 6% Mn, respectively, and the measured elastic modulus values lie between 27 and 33 GPa, which was close to E values calculated by Eqs. (3), (5) and (7). The samples did not exhibit a clear plastic yield stage (plateau stage) because pore walls deformed plastically (due to pores sliding each other). Foams have pre-existing micro flaws in pore walls, which decrease its strength. In the compressive test, macroscopic crack propagation resulted in an abrupt load drop (Fig. 14). The fluctuating stress–strain behavior of the samples occurs due of the brittle nature of the pore walls, which also lead to a lower degree of compaction [35]. According to Gibson and Ashby [15], density is the most important variable in deciding the properties of a porous sample by controlling its peak stress and elastic modulus. The morphology of pore walls and pore size has little effect on the strength of a porous material [53], but thicker pore walls and smaller pore diameters lead to higher elastic modulus (stiffness) and compressive strength. When foams are synthesized through milling, the work-hardening affects the particle packing characteristics modifying its densification in sintering stage of powder metallurgy [54].

4. Conclusions

The Ti–34Nb–29Ta–xMn (x: 2, 4 and 6 wt.% Mn) alloys were formed through mechanical alloying. The energy given by MA process was high enough to increase the solubility among Ti, Nb, Ta and Mn elements. The increased surface energy (due to decreased crystallite size) and elastic strain energy (due to increase in dislocation density) were responsible for the increase in solubility levels. Also 50 h milling produced a mixed of crystalline and amorphous phases.

Foams showed a non-homogeneous distribution of macro pores and micro pores with irregular shape. The macro pores produced by the space holder are smaller than 600 μm while the micro pores produced by sintering process are smaller than 20 μm. The macro and micro pores showed suitable features to promote cell adhesion and bone growth.

Measured elastic moduli of foams were around 30 GPa. This value lies in the upper range of elastic modulus of cortical bones. The elastic moduli determined by several models gave values very close to the measured ones. From the obtained results, synthesized metallic foams have a great potential for application as biomaterial.

Acknowledgments

The authors would like to acknowledge financial support from FONDECYT project no 1130417 and Universidad Técnica Federico Santa María project no 211225.

References

[1] M. Geetha, A.K. Singh, R. Asokamani, A.K. Gogia, Prog. Mater. Sci. 54 (2009) 397–425.
[2] M. Niinomi, Sci. Technol. Adv. Mater. 4 (2003) 445–454.
[3] J. Xiong, Y. Li, X. Wang, P. Hodgson, C.e. Wen, Acta Biomater. 4 (2008) 1963–1968.
[4] N. Nomura, T. Kohama, I.H. Oh, S. Hanada, A. Chiba, M. Kanehira, K. Sasaki, Mater. Sci. Eng. C 25 (2005) 330–335.
[5] X. Liu, P.K. Chu, C. Ding, Mater. Sci. Eng. R. Rep. 47 (2004) 49–121.
[6] G. Luthering, J. Williams, Springer-Verlag, 2003.
[7] K.L. Wapner, Clin. Orthop. Relat. Res. 271 (1991) 12–20.
[8] S. Nag, R. Banerjee, H.L. Fraser, Mater. Sci. Eng. C 25 (2005) 357–362.
[9] E. Eisenbarth, D. Velten, M. Müller, R. Thull, J. Breme, Biomaterials 25 (2004) 5705–5713.
[10] E.B. Taddei, V.A.R. Henriques, C.R.M. Silva, C.A.A. Cairo, Mater. Sci. Eng. C 24 (2004) 683–687.
[11] I. Kohlstadt, Scientific Evidence for Musculoskeletal, Bariatric, and Sports Nutrition, CRC Press, 2006.
[12] R. Nicula, F. Lüthen, M. Stir, B. Nebe, E. Burkel, Biomol. Eng. 24 (2007) 564–567.
[13] M. Niinomi, Metall. Mater. Trans. A 33 (2002) 477–486.
[14] E.-S. Kim, Y.-H. Jeong, H.-C. Choe, W.A. Brantley, Thin Solid Films 549 (2013) 141–146.
[15] L.J. Gibson, M.F. Ashby, Cellular Solids: Structure and Properties, Cambridge University Press, New York, NY, 1997.
[16] L.F. Nielsen, J. Am. Ceram. Soc. 67 (1984) 93–98.
[17] F.P. Knudsen, J. Am. Ceram. Soc. 42 (1959) 373–397.
[18] R.M. Spriggs, J. Am. Ceram. Soc. 44 (1961) 628–629.
[19] K. Phani, S. Niyogi, J. Mater. Sci. 22 (1987) 257–263.
[20] W. Pabst, E. Gregorová, J. Mater. Sci. 39 (2004) 3501.
[21] G.E. Ryan, A.S. Pandit, D.P. Apatsidis, Biomaterials 27 (2006) 2651–2670.
[22] Y. Torres, J. Pavón, I. Nieto, J.A. Rodríguez, Metall. Mater. Trans. B 42 (2011) 891–900.
[23] Y. Torres, S. Lascano, J. Bris, J. Pavón, J.A. Rodriguez, Mater. Sci. Eng. C 37 (2014) 148–155.

[24] Y. Torres, J.J. Pavón, J.A. Rodríguez, J. Mater. Process. Technol. 212 (2012) 1061–1069.
[25] Y. Torres, J.A. Rodríguez, S. Arias, M. Echeverry, S. Robledo, V. Amigó, J.J. Pavón, J. Mater. Sci. 47 (2012) 6565–6576.
[26] C. Suryanarayana, Mechanical Alloying and Milling, CRC Press, 2004.
[27] D. Zhang, Prog. Mater. Sci. 49 (2004) 537–560.
[28] A.A. Nazarov, A.E. Romanov, R.Z. Valiev, Scr. Mater. 34 (1996) 729–734.
[29] C. Suryanarayana, A. Inoue, Bulk Metallic Glasses, CRC Press, 2011.
[30] N. Al-Aqeeli, C. Suryanarayana, M.A. Hussein, J. Appl. Phys. 114 (2013) 153512–153514.
[31] Y. Gu, C. Goh, L. Goi, C. Lim, A. Jarfors, B. Tay, M. Yong, Mater. Sci. Eng. A 392 (2005) 222–228.
[32] C. Suryanarayana, I. Seki, A. Inoue, J. Non-Cryst. Solids 355 (2009) 355–360.
[33] S. Sharma, C. Suryanarayana, J. Appl. Phys. 102 (2007) 083544.
[34] K. Goi, D. Butler, A. Jarfors, J. Yong, D. Lim, Mater. Sci. Eng. A 475 (2008) 45–51.
[35] A. Nouri, P. Hodgson, C. Wen, Acta Biomater. 6 (2010) 1630–1639.
[36] A. Ibrahim, F. Zhang, E. Otterstein, E. Burkel, Mater. Des. 32 (2011) 146–153.
[37] F. Zhang, E. Otterstein, E. Burkel, Adv. Eng. Mater. 12 (2010) 863–872.
[38] M. Bram, C. Stiller, H.P. Buchkremer, D. Stover, H. Bauer, Adv. Eng. Mater. 2 (2000) 196–199.
[39] C. Wen, Y. Yamada, P. Hodgson, Mater. Sci. Eng. C 26 (2006) 1439–1444.
[40] Y.-Q. Wang, J. Tao, J.-l. Zhang, T. Wang, Trans. Nonferrous Metals Soc. China 21 (2011) 1074–1079.
[41] C. Xiang, Y. Zhang, Z. Li, H. Zhang, Y. Huang, H. Tang, Procedia Eng. 27 (2012) 768–774.
[42] X. Rao, C. Chu, Y. Zheng, J. Mech. Behav. Biomed. Mater. 34 (2014) 27–36.
[43] A. Bansiddhi, T. Sargeant, S. Stupp, D. Dunand, Acta Biomater. 4 (2008) 773–782.
[44] A.L. Gavzeo, P.B. Budberg, S.A. Minayeva, Niobium–Tantalum–Titanium Ternary Alloy Phase Diagram, ASM Alloy Phase Diagrams Center, 2007.
[45] F.H. Cocks, R.M. Rose, J. Wulff, Niobium–Tantalum–Titanium Ternary Alloy Phase Diagram, ASM Alloy Phase Diagrams Center, 2007.
[46] L. Na, W.H. Warnes, IEEE Trans. Appl. Supercond. 11 (2001) 3800–3803.
[47] X. Tang, T. Ahmed, H. Rack, J. Mater. Sci. 35 (2000) 1805–1811.
[48] F. Prima, P. Vermaut, G. Texier, D. Ansel, T. Gloriant, Scr. Mater. 54 (2006) 645–648.
[49] D.L. Moffat, D.C. Larbalestier, MTA 19 (1988) 1687–1694.
[50] A. Cremasco, P.N. Andrade, R.J. Contieri, E.S.N. Lopes, C.R.M. Afonso, R. Caram, Mater. Des. 32 (2011) 2387–2390.
[51] K. Zhu, C. Li, Z. Zhu, C. Liu, J. Mater. Sci. 42 (2007) 7348–7353.
[52] X. Neil Dong, X. Edward Guo, J. Biomech. 37 (2004) 1281–1287.
[53] T. Nieh, K. Higashi, J. Wadsworth, Mater. Sci. Eng. A 283 (2000) 105–110.
[54] R.M. German, Sintering Theory and Practice, in: Randall M. German (Ed.) Wiley-VCH, ISBN: 0-471-05786-X January 1996, p. 568 (1).